

pubs.acs.org/JACS Article

# Visible-Light-Driven Nitrogen Fixation Catalyzed by Bi<sub>5</sub>O<sub>7</sub>Br Nanostructures: Enhanced Performance by Oxygen Vacancies

Peishen Li, Ziang Zhou, Qiang Wang,\* Ming Guo, Shaowei Chen,\* Jingxiang Low, Ran Long, Wen Liu,\* Peiren Ding, Yunyun Wu, and Yujie Xiong\*



Cite This: J. Am. Chem. Soc. 2020, 142, 12430-12439



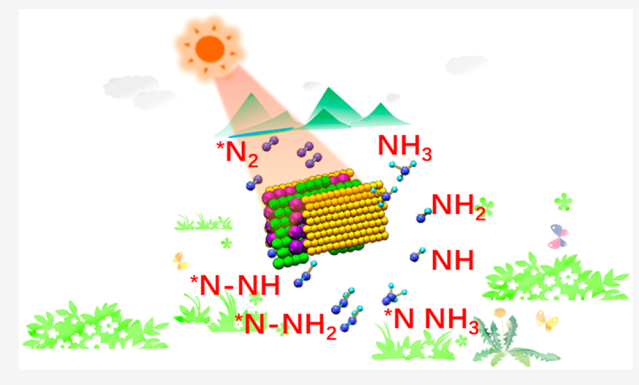
**ACCESS** 

Metrics & More

Article Recommendations

s Supporting Information

**ABSTRACT:** Photocatalytic nitrogen fixation represents a green alternative to the conventional Haber–Bosch process in the conversion of nitrogen to ammonia. In this study, a series of Bi<sub>5</sub>O<sub>7</sub>Br nanostructures were synthesized via a facile, low-temperature thermal treatment procedure, and their photocatalytic activity toward nitrogen fixation was evaluated and compared. Spectroscopic measurements showed that the tubular Bi<sub>5</sub>O<sub>7</sub>Br sample prepared at 40 °C (Bi<sub>5</sub>O<sub>7</sub>Br-40) exhibited the highest electron-transfer rate among the series, producing a large number of O<sub>2</sub><sup>-</sup> radicals and oxygen vacancies under visible-light photoirradiation and reaching a rate of photocatalytic nitrogen fixation of 12.72 mM·g<sup>-1</sup>·h<sup>-1</sup> after 30 min of photoirradiation. The reaction dynamics was also monitored by in situ infrared measurements with a synchrotron radiation light source, where the transient difference between signals in the dark and



under photoirradiation was analyzed and the reaction pathway of nitrogen fixation was identified. This was further supported by results from density functional theory calculations. The reaction energy of nitrogen fixation was quantitatively estimated and compared by building oxygen-enriched and anoxic models, where the change in the oxygen vacancy concentration was found to play a critical role in determining the nitrogen fixation performance. Results from this study suggest that Bi<sub>5</sub>O<sub>7</sub>Br with rich oxygen vacancies can be used as a high-performance photocatalyst for nitrogen fixation.

## **■ INTRODUCTION**

Nitrogen is one of the most abundant elements on earth, mostly as nitrogen gas  $(N_2)$  in the atmosphere.  $^{1-3}$  Ammonia synthesis is an important reaction in the natural fixation of nitrogen. However, industrial nitrogen fixation, such as the Haber-Bosch process, not only requires high temperature and high pressure but also consumes a large amount of hydrogen.<sup>4,5</sup> Recently, photocatalytic nitrogen fixation has been attracting extensive interest thanks to its energy and environmental advantages, 4-7 where artificial photosynthesis is exploited for the direct production of NH<sub>3</sub> from N<sub>2</sub> and H<sub>2</sub>O under sunlight with the assistance of an appropriate catalyst.8 However, the efficiency of photocatalytic nitrogen fixation is generally low and limited by two major factors: (a) the reduction of one N2 molecule requires the transfer of six electrons, but most catalysts cannot produce abundant electrons due to the high recombination rate of photogenerated electrons and holes and (b) N<sub>2</sub> adsorption is a necessary step for the catalytic reaction, but most catalysts exhibit only weak N2 adsorption. Thus, the design and engineering of effective catalysts with high N2 adsorption and efficient separation of photogenerated electron-hole pairs is key to an improved performance of photocatalytic nitrogen fixation.4

Recent research has shown that BiOX (X = Cl and Br) materials exhibit excellent photocatalytic activity toward nitrogen fixation due to their unique layer structures and appropriate band gaps. Among these, layered bismuth oxybromide (BiOBr) is of particular interest because the inherent internal static electric field can improve the diffusion coefficient (D) of electron—hole pairs, leading to enhanced carrier mobility and a reduced recombination rate. Furthermore, for bismuth oxybromide-based semiconductors, oxygen vacancies (OVs) with abundant localized electrons on the surface have been demonstrated to facilitate the adsorption and activation of  $N_2$ . Thus, one can envision that the design and engineering of bismuth oxybromide nanostructures may be exploited to markedly advance the photocatalytic fixation of nitrogen.

Received: May 8, 2020 Published: June 12, 2020





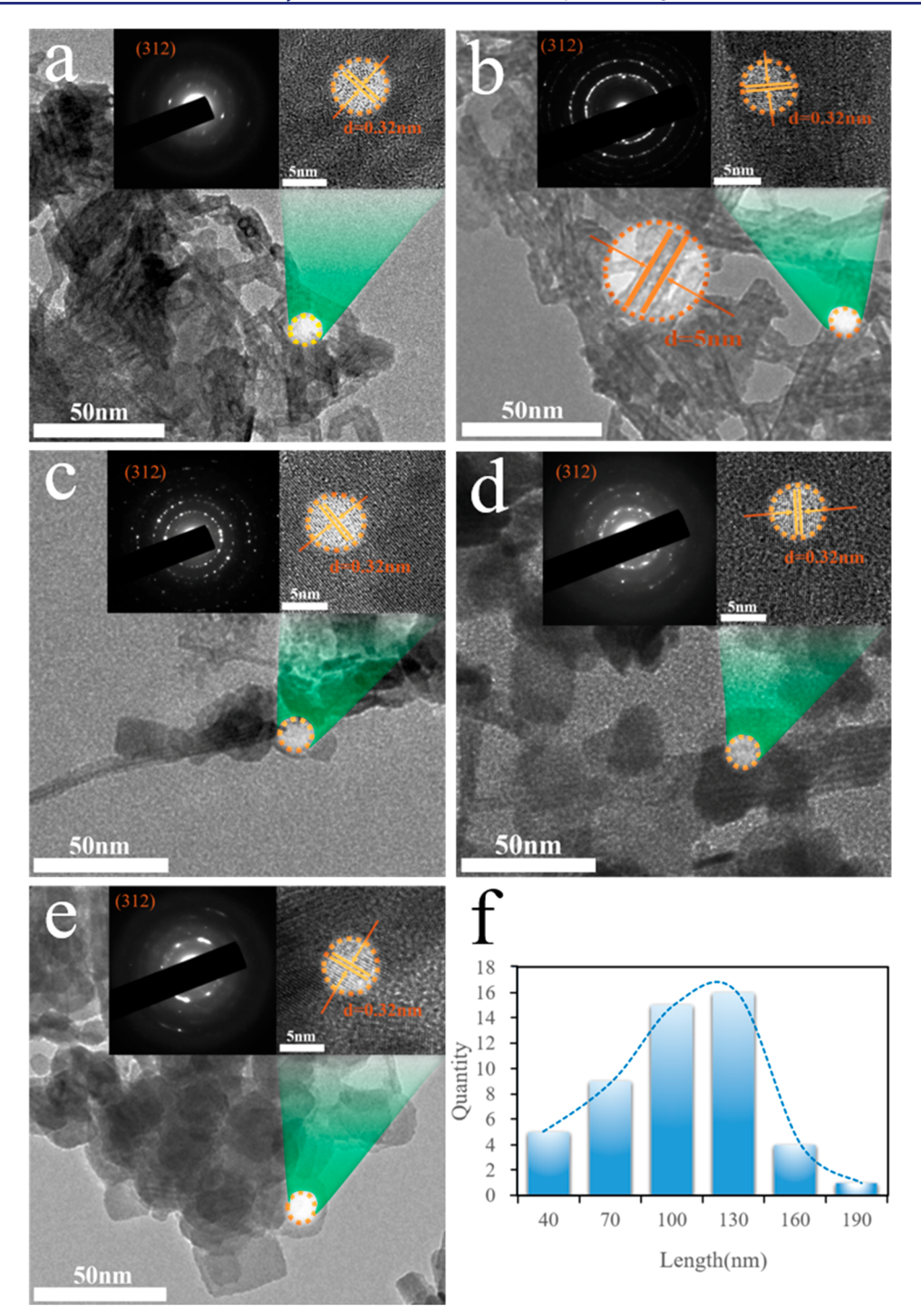


Figure 1. Representative TEM images of (a)  $Bi_5O_7Br-20$ , (b)  $Bi_5O_7Br-40$ , (c)  $Bi_5O_7Br-60$ , (d)  $Bi_5O_7Br-80$ , and (e)  $Bi_5O_7Br-100$ . The left insets are the corresponding SAED patterns, and the right insets are the respective HRETM images. (f) Length distributions of 50  $Bi_5O_7Br$  nanotubes randomly selected from the  $Bi_5O_7Br-40$  sample in panel (b).

Notably, because the recombination of photogenerated electron—hole pairs may occur in the interior of the semiconductors before they reach the surface to initiate reactions, various forms of nanostructures, such as nanoparticles, nanotubes, nanowires, and nanosheets, have been prepared to shorten the migration distance. <sup>17,18</sup> In fact, a range of strategies have been employed to engineer the BiOBr structure, such as morphological control, <sup>19,20</sup> exposure of select crystalline facets, <sup>21</sup> and heterologous hybridization. <sup>22–27</sup> For instance, Di et al. <sup>28</sup> prepared Bi<sub>4</sub>O<sub>5</sub>Br<sub>2</sub> ultrathin nanosheets via

an ionic-liquid-assisted solvothermal method under pH control, which effectively increased the electron-transfer rate and greatly improved the photocatalytic degradation of ciprofloxacin. Wang et al. 19 reported a novel low-temperature method for the water-assisted self-assembly of  ${\rm Bi}_5{\rm O}_7{\rm Br}$  nanotubes (average cross-sectional diameter 5 nm), which diminished the electron-migration distance and increased the electron-transfer rate, resulting in a significant increase in the rate of nitrogen fixation. However, optimization of the material structure and hence the fixation performance remain lacking.

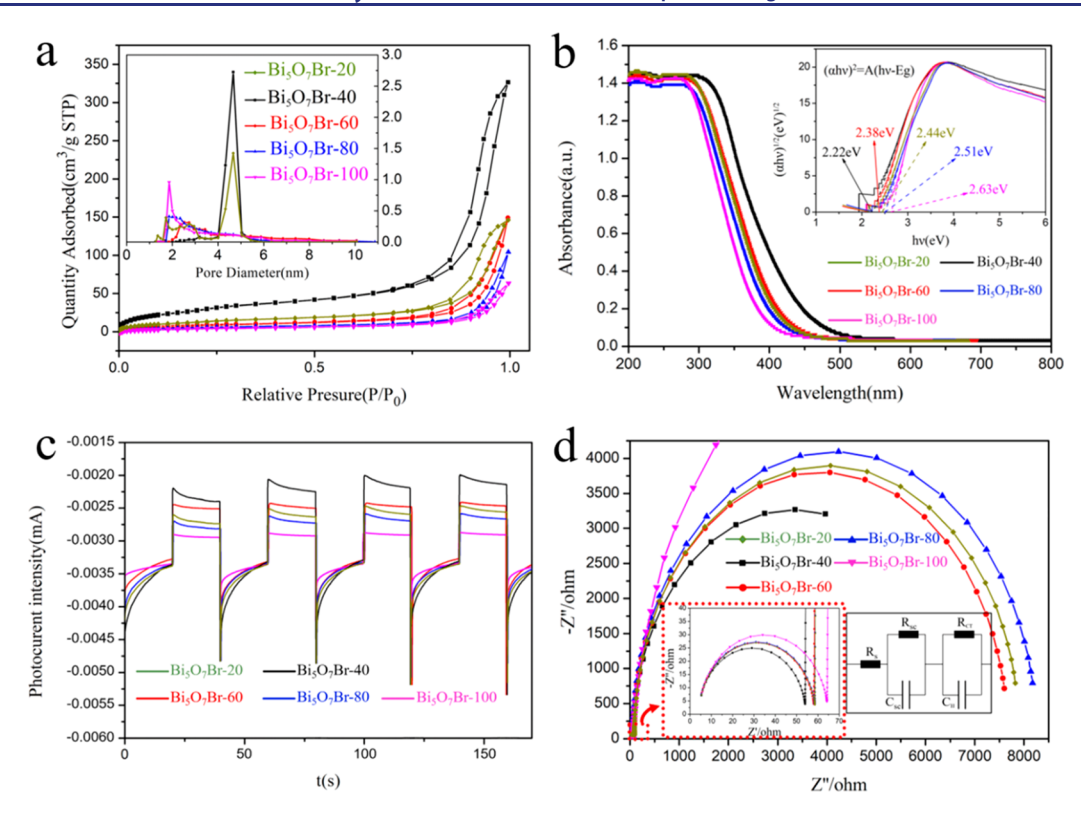


Figure 2. (a) Nitrogen adsorption—desorption isotherms of the series of  $Bi_5O_7Br$  samples. The inset depicts the corresponding pore size distribution curves. (b) UV—vis diffuse reflectance spectra for the various  $Bi_5O_7Br$  samples. The inset shows the  $(\alpha h \nu)^{1/2}$  versus  $h \nu$  curves. (c) Transient photocurrent response and (d) impedance curves of the various  $Bi_5O_7Br$  samples. In panel (d), the left inset is a close-up image of the boxed area, whereas the right inset is the equivalent circuit used to fit the impedance data, where  $R_S$  is the series resistance (including the material resistance and contact resistance of the test system),  $R_{SC}$  is the charge-transfer resistance at the  $Bi_5O_7Br$ /electrode interface, and  $R_{CT}$  is the charge-transfer resistance at the  $Bi_5O_7Br$ /electrode interface (i.e., the internal capacitance of the material), and  $C_H$  is the capacitance of the  $Bi_5O_7Br$ /electrolyte interface. Symbols are experimental data, and solid curves are the corresponding fits.

In this study, a series of Bi<sub>5</sub>O<sub>7</sub>Br nanostructures were prepared by a facile thermal procedure in a water bath at controlled temperatures (20 to 100 °C) and exhibited apparent photocatalytic activity toward nitrogen fixation under visible light photoirradiation (>400 nm). Among the series, the sample prepared at 40 °C stood out as the best catalyst, which coincided with the smallest band gap, largest OV content, highest photocurrents, best diffusion of photogenerated electron-hole pairs, and lowest charge-transfer resistance. The dynamics of nitrogen fixation was also monitored by in situ infrared spectroscopy using a synchrotron radiation source. It was found that the adsorption of nitrogen was indeed facilitated by the OVs, which played a key role in the determination of the photocatalytic activity, in good agreement with results from density functional theory (DFT) calculations. Taken together, these results highlight the significance of structural engineering in the development of high-efficiency photocatalysts toward nitrogen fixation.

#### EXPERIMENTAL SECTION

**Material Preparation.** All chemicals were of analytical purity, purchased from Aladdin and used without further purification. Deionized water was used in all experiments.

**Preparation of Bi<sub>5</sub>O<sub>7</sub>Br Nanostructures.** Bi<sub>5</sub>O<sub>7</sub>Br nanostructures were synthesized by a water-induced self-assembly method. In brief, 50 mL of an ammonia solution and 3 mmol of Bi(NO<sub>3</sub>)<sub>3</sub>·SH<sub>2</sub>O were added to five beakers, which were then heated to five different temperatures: 20, 40, 60, 80, and 100 °C. After 10 min of heating, an equal amount of KBr was added to the beakers under magnetic mixing, followed by the dropwise addition of 5 mL of deionized water

until a translucent solution was obtained. The resulting mixtures were heated for 10 days before being separated by centrifugation at 10 000 rpm, rinsed with cyclohexane and absolute ethanol several times, and finally dried at 60 °C for 12 h.  $^{27}$  The obtained products were denoted as Bi<sub>5</sub>O<sub>7</sub>Br-T, with T being the heating temperature.

Characterization. The material morphologies were analyzed by high-resolution transmission electron microscopy measurements (HRTEM, JEOL 2010 F). X-ray diffraction (XRD) patterns were acquired with a Bruker D8 Advance X-ray diffractometer equipped with Cu K<sub>a</sub> radiation ( $\lambda = 1.5418$  Å). X-ray photoelectron spectroscopy (XPS) measurements were carried out with a Thermo Kratos Axis Supra instrument. All binding energies were referenced to the C 1s peak at 284.6 eV. Raman spectra were recorded at room temperature using a micro Raman spectrometer (Renishaw RM-1000) in backscattering geometry with a 532 nm laser as the excitation source. Electron spin resonance (ESR) spectra were collected with a Bruker ER200-SRC-10/12 spectrometer. Because of the chemical reactivity of superoxide radicals  $(O_2^{-})$  in water, 5,5dimethyl-1-pyrroline N-oxide (DMPO) was used to trap O2. in methanol, whereas hydroxyl radicals did not react with water so the ESR signals were acquired in water. The OV signals were detected directly with solid Bi<sub>5</sub>O<sub>7</sub>Br powders. Brunauer-Emmett-Teller (BET) surface areas were analyzed with a nitrogen adsorption apparatus (BET, Mike ASAP2020). Optical absorbance and UV-vis diffuse reflectance spectra (DRS) were measured with a Thermo UV-2600 UV-vis spectrophotometer. Electrochemical impedance spectra (EIS) and transient photocurrents were acquired with a CHI 760e electrochemical workstation. Photoluminescence spectroscopy measurements were conducted with an Edinburgh Instruments FLS980 Spectrometer.

Photocatalysis. Photocatalytic N<sub>2</sub> fixation experiments were conducted at ambient temperature using a 300 W Xe lamp with a

400 nm cutoff filter located approximately 10 cm from the sample. First, 0.025 g of the  $Bi_sO_7Br$  samples prepared above was dispersed in 100 mL of deionized water in a cell equipped with water circulation. Second, the mixture was continuously stirred in the dark and bubbled with high-purity  $N_2$  at a flow rate of 50 mL·min $^{-1}$  for 30 min before being exposed to visible light irradiation ( $\lambda > 400$  nm). An aliquot (3 mL) of the reaction solution was removed every 3 min. The concentration of  $NH_4^+$  was quantified by using Nessler's reagent as a chromogenic agent that can be detected at 420 nm with a Thermo UV-2600 UV—vis spectrometer.  $^{1,27}$ 

**DFT Calculations.** First-principles calculations in the framework of DFT, including structural and electronic performances, were carried out on the basis of the Cambridge Sequential Total Energy Package (CASTEP). The exchange-correlation functional under the generalized gradient approximation (GGA) and the revised Perdew–Burke–Ernzerhof functional were adopted to describe the electron–electron interactions. An energy cutoff of 400 eV and a k-point sampling set of  $1 \times 2 \times 1$  were chosen for the calculations, with a force tolerance of  $3 \times 10^{-2}$  eV Å $^{-1}$ , an energy tolerance of  $1.0 \times 10^{-5}$  eV per atom, and a maximum displacement of  $1.0 \times 10^{-3}$  Å.

A pristine  $Bi_5O_7Br$  (1) surface, which contains 104 atoms (including 40 Bi, 8 Br, and 56 O atoms), was used in the calculations, in comparison to  $Bi_5O_7Br$  with 1 oxygen vacancy ( $Bi_5O_7Br$ —O, which contained 40 Bi, 8 Br, and 55 O atoms) and  $Bi_5O_7Br$  with one additional oxygen ( $Bi_5O_7Br$ +O, which consisted of 40 Bi, 8 Br, and 57 O atoms). The oxygen defects were located near the adsorption site. The core electrons were treated with ultrosoft pseudopotentials. The vacuum space along the z direction was set to 15 Å to avoid interactions between the two slab models. The bottom atomic layers were fixed, and the rest of the atomic layers and absorbed molecules were relaxed during all calculations. The Gibbs free energy for all  $N_2$  reduction reactions was defined as follows

$$\Delta G = \Delta E + \Delta Z P E - T \Delta S \tag{1}$$

where  $\Delta E$ ,  $\Delta ZPE$ , T, and  $\Delta S$  are the adsorption energy, zero-point energy difference, reaction temperature, and entropy difference between the adsorbed state and the gas phase, respectively.

The adsorption energy  $\Delta E$  of molecule A on the substrate surface is defined as

$$\Delta E = E_{*A} - (E_* + E_A) \tag{2}$$

where  $E_{*A}$ ,  $E_{A}$ , and  $E_{*}$  denote the energies of surface-adsorbed molecule A, free molecule A, and the bare substrate, respectively.

#### RESULTS AND DISCUSSION

The sample structures were first examined by TEM measurements. It can be seen from Figure 1 that the samples prepared at temperatures of (a) 20, (b) 40, and (c) 60 °C all exhibited rather well-defined nanotubular structures with a crosssectional diameter of ca. 5 nm and a length of ca. 100 nm (mostly between 80 and 150 nm, Figure 1f). Yet at higher temperatures, a plate-like morphology became increasingly apparent, as manifested in the (d) Bi<sub>5</sub>O<sub>7</sub>Br-80 and (e) Bi<sub>5</sub>O<sub>7</sub>Br-100 samples, with a side length of 20-30 nm. This structural evolution suggests that water-assisted self-assembly at low temperatures led to the formation of nanotubules, 1 which became ruptured into flaky structures at higher temperatures. Nevertheless, in high-resolution TEM measurements (right insets to panels a-e), all samples show clearly defined lattice fringes with an interplanar spacing of 0.32 nm, which can be assigned to the (312) crystalline facets of Bi<sub>5</sub>O<sub>7</sub>Br, <sup>27,32</sup> consistent with the patterns of selected-area electron diffraction (SAED, left insets to panels a-e).

The porosity of the samples was then examined by nitrogen adsorption—desorption measurements. From the adsorption isotherms in Figure 2a, the BET specific surface area was found to vary among the series of samples: 45 m<sup>2</sup> g<sup>-1</sup> for Bi<sub>5</sub>O<sub>7</sub>Br-20,

101 m² g⁻¹ for Bi₅O¬Br-40, 30 m² g⁻¹ for Bi₅O¬Br-60, 22 m² g⁻¹ for Bi₅O¬Br-80, and 13 m² g⁻¹ for Bi₅O¬Br-100. That is, the sample prepared at 40 °C exhibited the largest surface area among the series. That the pore size distributions (Figure 2a inset), one can see that the pores primarily fall into two size ranges (1.5 to 3 nm and 4 to 5 nm), and with increasing synthesis temperature, the fraction of the larger pores decreases whereas the fraction of the smaller pores increases. This is consistent with the morphological variation of the samples, which show a tubular structure for samples prepared at low temperatures but a flaky structure at high temperatures (Figure 1). The samples in the samples in the samples prepared at low temperatures but a flaky structure at high temperatures (Figure 1).

The formation of Bi<sub>5</sub>O<sub>7</sub>Br was further confirmed by XRD measurements. From Figure S1, a series of diffraction peaks can be identified at  $2\theta = 24.46$ , 30.18, 32.64, 46.76, 51.18, and 56.62°, which can be readily indexed to the (312), (004), (600), (604), (314), and (912) facets of the tetragonal phase of Bi<sub>5</sub>O<sub>7</sub>Br (JCPDS card no. 038-0493). 34-37 No other diffraction peaks can be observed, indicating that the samples were a pure crystalline phase. Consistent results were obtained in Raman spectroscopic measurements (Figure S2), where all Bi<sub>5</sub>O<sub>7</sub>Br samples showed two major vibrational bands at ca. 85 and  $125 \text{ cm}^{-1}$  due to the  $A_{1g}$  and  $E_{g}$  modes of Bi-Br stretching vibrations, respectively.<sup>38</sup> In UV-vis diffuse reflectance measurements (Figure 2b), the Bi<sub>5</sub>O<sub>7</sub>Br samples can be seen to exhibit a rather well-defined absorption edge, which redshifted from 430 to 530 nm when the sample was prepared at increasing temperature. In fact, from the Tauc plot in the Figure 2b inset, the band gap can be estimated to be 2.44 eV for Bi<sub>5</sub>O<sub>7</sub>Br-20, 2.22 eV for Bi<sub>5</sub>O<sub>7</sub>Br-40, 2.38 eV for Bi<sub>5</sub>O<sub>7</sub>Br-60, 2.51 eV for Bi<sub>5</sub>O<sub>7</sub>Br-80, and 2.63 eV for Bi<sub>5</sub>O<sub>7</sub>Br-100. That is, the Bi<sub>5</sub>O<sub>7</sub>Br-40 sample exhibited the smallest band gap in

Photoelectrochemistry and electrochemical impedance measurements were then carried out to examine the dynamics of photogenerated electrons in the Bi<sub>5</sub>O<sub>7</sub>Br samples. Under the irradiation of a 300 W Xe lamp that provided simulated solar light radiation (100 mW cm<sup>-2</sup>), photocurrent curves were acquired by linear sweep voltammetry (LSV) scans under chopped illumination with a fixed time interval. From Figure 2c, one can see that the Bi<sub>5</sub>O<sub>7</sub>Br-40 sample exhibited the highest photocurrent among the series, 12,38,39 with an instantaneous photocurrent response of about 1.5  $\mu$ A, in comparison to 0.9-1.1  $\mu$ A for other samples. It should be noted that a higher photogenerated current suggests a more efficient separation of photogenerated electron-hole pairs. This indicates that Bi<sub>5</sub>O<sub>7</sub>Br-40 stood out as the best photocatalyst among the series of samples. Consistent results were obtained in electrochemical impedance spectroscopy studies under AM 1.5 G illumination. The results are shown in Figure 2d and are fitted with the equivalent circuit in the right inset, with the fitting results summarized in Table 1. It can be

Table 1. Summary of the Fitting Results of Impedance Data of the  $Bi_5O_7Br$  Series

	$R_{\rm S} \; (\Omega)$	$R_{\mathrm{SC}}\left(\Omega ight)$	$R_{\mathrm{CT}}\left(\Omega\right)$
$\mathrm{Bi_5O_7Br\text{-}20}$	4.3	54.6	7846
$Bi_5O_7Br-40$	4.0	54.2	6537
Bi <sub>5</sub> O <sub>7</sub> Br-60	4.3	54.3	7611
$Bi_5O_7Br-80$	4.3	54.9	8194
$Bi_5O_7Br-100$	4.7	59.5	15 140

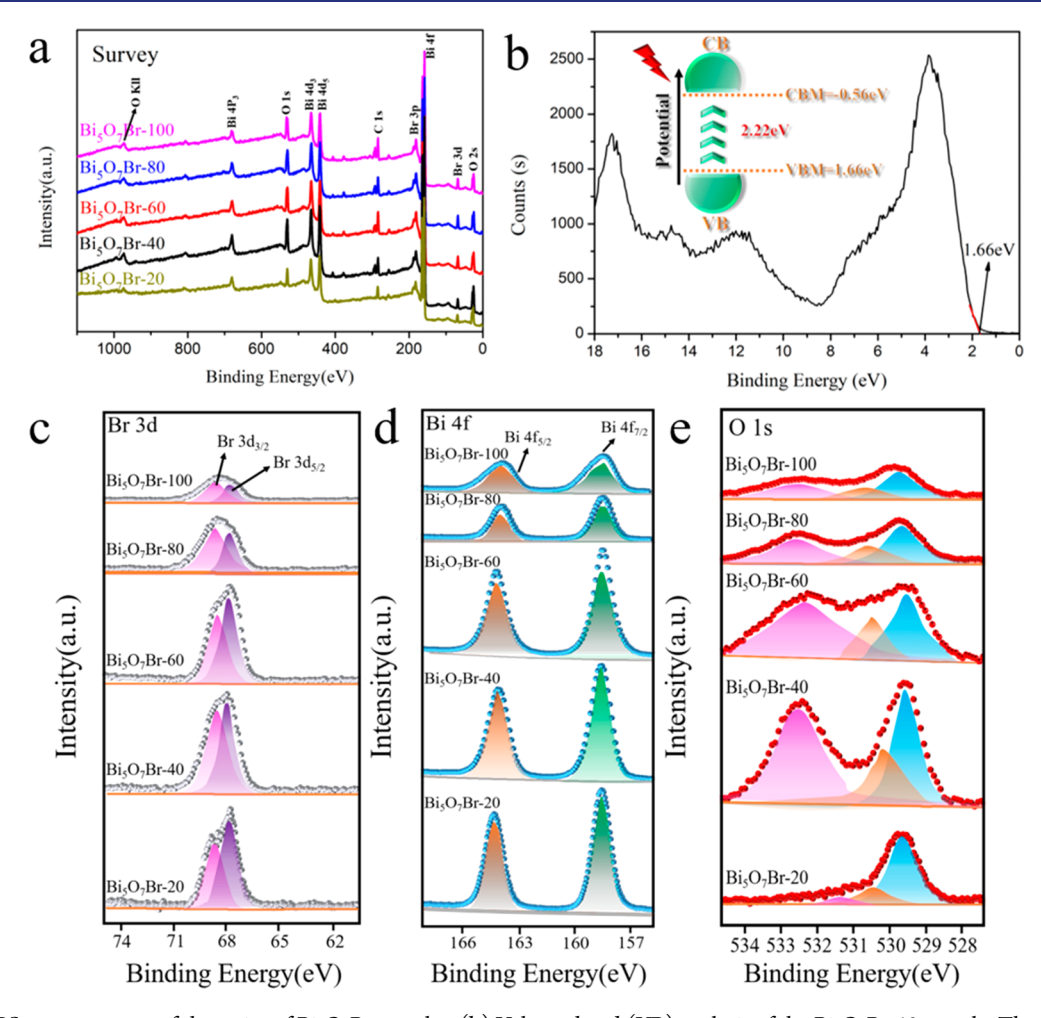


Figure 3. (a) XPS survey spectra of the series of  $Bi_5O_7Br$  samples. (b) Valence-band (VB) analysis of the  $Bi_5O_7Br$ -40 sample. The inset is a diagram of the electronic energy levels. High-resolution scans of the (c)  $Bi_5O_7Br$  samples. Dotted curves are experimental data, and shaded peaks are deconvolution fits.

seen that Bi<sub>S</sub>O<sub>7</sub>Br-40 exhibited the lowest charge-transfer resistance ( $R_{\rm CT}$ , 6537  $\Omega$ ) among the series. This correlates well with the highest photocurrents observed in Figure 2c.<sup>40</sup> In addition, one can see that Bi<sub>S</sub>O<sub>7</sub>Br-40 also exhibited the lowest internal resistance ( $R_{\rm S}$ , 4.0  $\Omega$ ) and interfacial resistance ( $R_{\rm SC}$ , 54.2  $\Omega$ ).

The elemental composition and valence state of the Bi<sub>5</sub>O<sub>7</sub>Br samples were then studied and compared by XPS measurements. Figure 3a shows the full survey spectra of the Bi<sub>5</sub>O<sub>7</sub>Br samples, where elements of Bi (157.25-166.34 eV), Br (66.03-70.58 eV), O (528.46-535.29 eV), and C (284.81 eV) can be readily identified. On the basis of the integrated peak areas, the atomic ratio of Bi/Br was estimated to be ca. 4.83, close to the stoichiometric ratio of Bi<sub>5</sub>O<sub>7</sub>Br. Results from XPS measurements can also be used to determine the energy of the valence band (VB).<sup>39</sup> From Figure 3b, the VB of the Bi<sub>5</sub>O<sub>7</sub>Br-40 sample can be calculated to be -0.56 eV versus NHE. This means that the conduction band (CB) lies at ca. +1.66 eV, considering a band gap of ca. 2.2 eV that was obtained from UV-vis measurements (Figure 2b). The corresponding high-resolution scans of the Br 3d electrons can be found in Figure 3c, where deconvolution yields two main peaks at 67.6 and 69.2 eV due to the  $3d_{3/2}$  and  $3d_{5/2}$ electrons of Br-. The high-resolution scans of the Bi 4f electrons are shown in Figure 3d, which entail two main peaks

at 158.7 and 163.9 eV, consistent with the  $4f_{7/2}$  and  $4f_{5/2}$  electrons of  $Bi^{3+}$ . In the O 1s scans (Figure 3e), there are three O species that can be ascribed to the lattice oxygen in the sample interior (529.5 eV), OVs (530.5 eV), and absorbed oxygen on the sample surface (532.2 eV).  $^{36,37}$  On the basis of the integrated peak areas, the OV concentration was found to vary among the series of samples:  $Bi_5O_7Br-40$  (14.6%) >  $Bi_5O_7Br-60$  (14.2%) >  $Bi_5O_7Br-100$  (11.9%) >  $Bi_5O_7Br-80$  (10.6%) >  $Bi_5O_7Br-20$  (9.5%). That is,  $Bi_5O_7Br-40$  exhibits the highest OV content in the series.

ESR measurements were then carried out to detect the formation of radical species and OVs. It can be seen that the quantities of  $O_2$ <sup>-</sup> (g=2.453, Figure 4a) and OV (g=2.001, Figure 4b) produced by  $Bi_5O_7Br-40$  upon photoirradiation were significantly higher than those in the dark. Consistent behaviors can be seen with other samples in the series, where  $Bi_5O_7Br-40$  produced the largest quantities of  $O_2$ <sup>-</sup> radicals and OVs (Figures S3 and S4), suggesting the most efficient separation of the photogenerated electron—hole pairs.  $^{38,39}$  Note that the production of a large number of OVs was conducive to  $N_2$  adsorption and fixation (vide infra).  $^{13,27,40,41}$  By contrast, no obvious hydroxyl radical signal was detected with the  $Bi_5O_7Br-40$  and  $Bi_5O_7Br-100$  samples in the dark or under photoirradiation (Figure S5).  $^{42}$ 

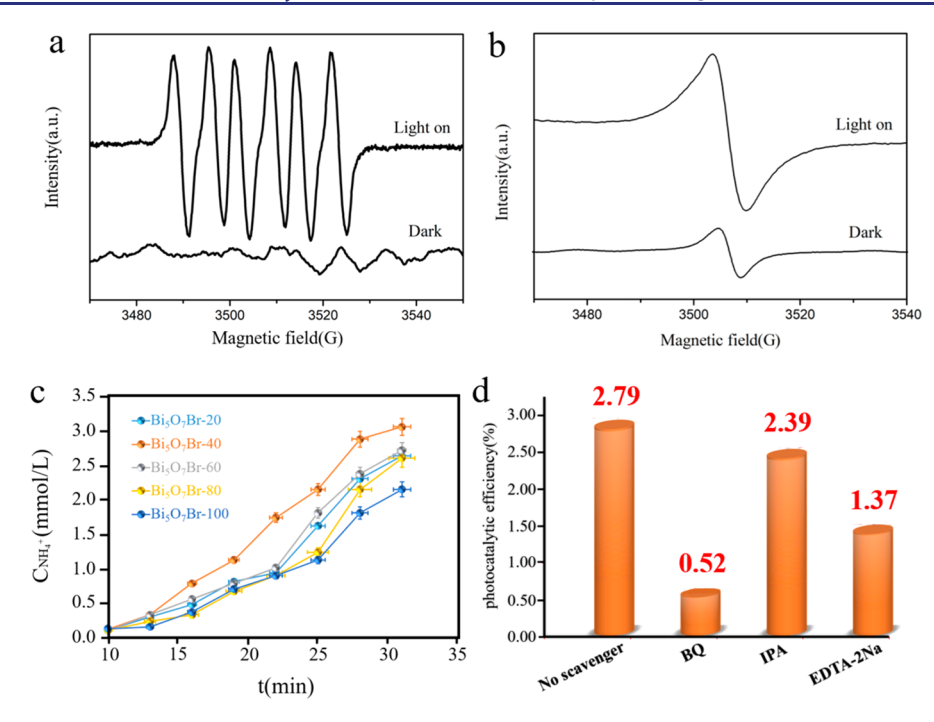


Figure 4. ESR spectra of (a)  $O_2$  radicals and (b) OVs produced by  $Bi_5O_7Br$ -40 in the dark and under visible light photoirradiation. (c) Amount of nitrogen fixation catalyzed by different  $Bi_5O_7Br$  samples with time. (d) Photocatalytic performance of nitrogen fixation by  $Bi_5O_7Br$ -40 (0.5 g·L<sup>-1</sup>) in the absence and presence of various radical scavengers after visible light photoirradiation for 30 min.

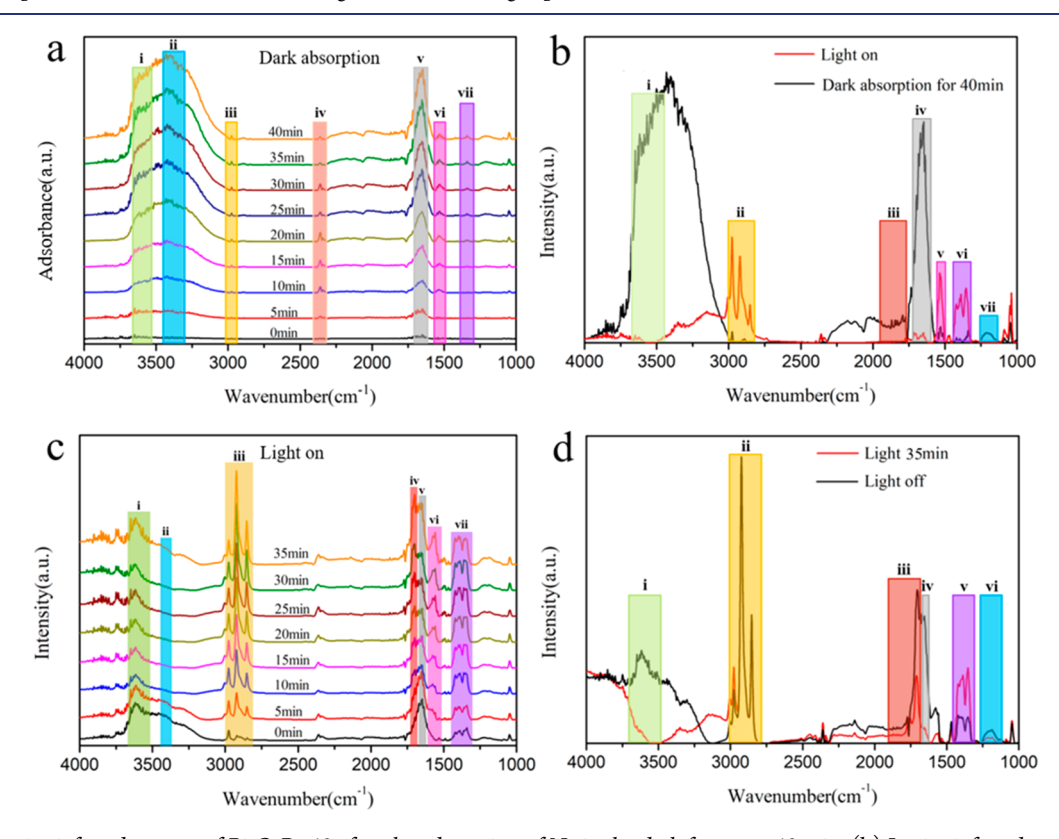


Figure 5. (a) In situ infrared spectra of  $Bi_5O_7Br$ -40 after the adsorption of  $N_2$  in the dark for up to 40 min. (b) In situ infrared spectra of  $Bi_5O_7Br$ -40 after adsorption in the dark for 40 min and then visible light photoirradiation being turned on. (c) In situ infrared spectra of  $Bi_5O_7Br$ -40 under visible light photoirradiation for up to 35 min. (d) In situ infrared spectra of  $Bi_5O_7Br$ -40 after visible light photoirradiation for 35 min, after which the light is turned off.

Consistent behaviors were observed in photoluminescence measurements. From Figure S6, all Bi<sub>5</sub>O<sub>7</sub>Br samples can be seen to exhibit a prominent emission peak at ca. 473 nm, and

the  ${\rm Bi_5O_7Br\text{-}40}$  sample displayed the lowest peak intensity among the series. Because electron—hole recombination is responsible for the photoluminescence emission, a low

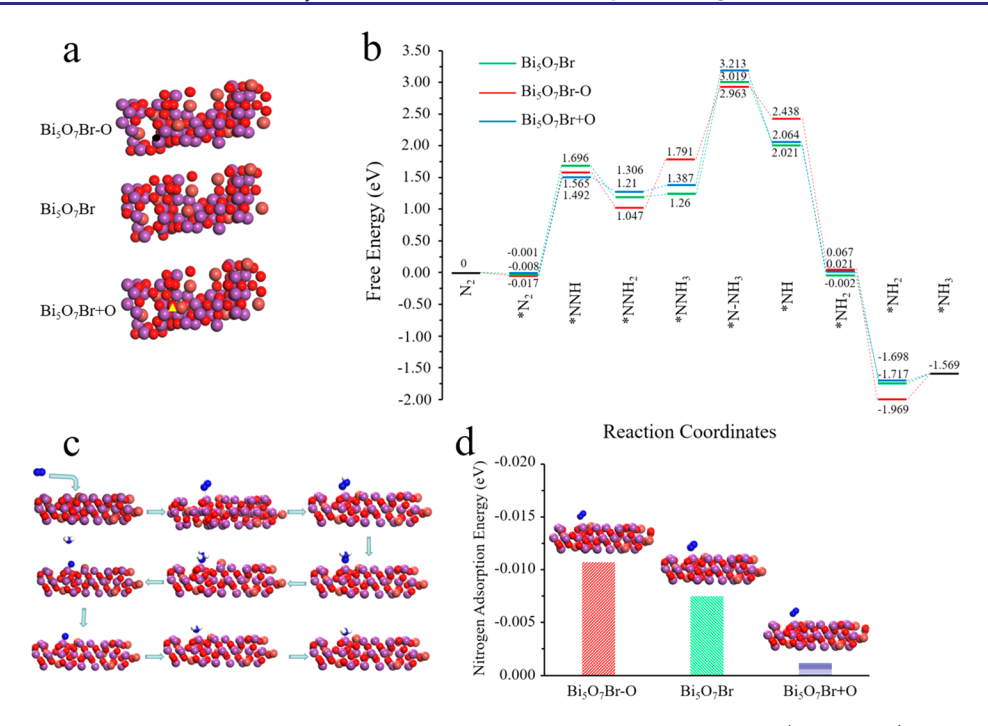


Figure 6. (a) Structural models of anoxic  $Bi_5O_7Br-O$ , pristine  $Bi_5O_7Br$ , and oxygen-enriched  $Bi_5O_7Br$  ( $Bi_5O_7Br+O$ ). The black circle represents the site of an oxygen vacancy, and the yellow triangle refers to the site of the additional oxygen. (b) Reaction energy diagram of nitrogen fixation catalyzed by  $Bi_5O_7Br-O$ ,  $Bi_5O_7Br$ , and  $Bi_5O_7Br+O$ . (c) Schematic pathway of nitrogen fixation. (d) Nitrogen adsorption energy (eV) on the surfaces of  $Bi_5O_7Br-O$ ,  $Bi_5O_7Br$ , and  $Bi_5O_7Br+O$ .

photoluminescence intensity implies a low recombination rate of photogenerated charge carriers. Taken together, one can see that the  ${\rm Bi_5O_7Br\text{-}40}$  sample displays the highest charge separation efficiency among the series, a unique feature that can facilitate the photocatalysis of nitrogen fixation.

Remarkably, the Bi $_5$ O $_7$ Br samples prepared above indeed exhibited apparent photocatalytic activity toward nitrogen fixation to ammonia under visible light illumination. The quantity of NH $_4$ <sup>+</sup> generated was quantified by using Nessler's reagent as a chromogenic probe (Figure S7). From Figure 4c, one can see that Bi $_5$ O $_7$ Br-40 produced the largest quantity of NH $_4$ <sup>+</sup> after 30 min of photoirradiation at 3.18 mM·L $^{-1}$ , and the rate of nitrogen fixation was estimated to be 12.72 mM·g $^{-1}$ h $^{-1}$ , which was 9.8 times those of other Bi $_5$ O $_7$ Br samples and 122.5 times those of relevant BiOBr catalysts reported in the literature (Table S1).

To unravel the roles of the various radicals generated in the photocatalytic process, benzoquinone (BQ), isopropanol (IPA), and ethylenediamine tetraacetic acid disodium salt (EDTA-2Na) were used as the respective scavengers for OVs, · OH¯, and O₂¯. From Figure 4d, it can be seen that after 30 min of visible light irradiation the addition of BQ and EDTA-2Na significantly inhibited nitrogen fixation, while only a slight decrease was observed with IPA. This suggests that O₂¯ and OVs were the two primary radicals involved in nitrogen fixation under visible light irradiation, with a minor contribution from ·OH¯. This is consistent with the lack of · OH¯ production, as manifested in ESR measurements (Figure S5).

The stability of the Bi<sub>5</sub>O<sub>7</sub>Br samples was then tested by cycling voltammetric measurements.<sup>47,48</sup> From Figure S8, one can see that after 500 cycles, the Bi<sub>5</sub>O<sub>7</sub>Br-40 sample showed the highest stability among the series, with virtually no change in the voltammetric curves, whereas a marked diminishment of

the voltammetric currents can be seen with other samples. <sup>49</sup> Consistent results were obtained in microscopic and spectroscopic measurements. From the SEM and TEM images in Figure S9, one can see that the  ${\rm Bi}_5{\rm O}_7{\rm Br}$ -40 sample exhibited no obvious change in the morphology before and after the stability test, and the XPS profiles (Figure S10) remained virtually invariant.

In order to unravel the photocatalytic mechanism of nitrogen fixation by the Bi<sub>5</sub>O<sub>7</sub>Br catalysts, in situ infrared spectroscopic measurements were carried out using a synchrotron radiation source. Figure 5a shows the IR spectra of N<sub>2</sub> adsorption on Bi<sub>5</sub>O<sub>7</sub>Br-40 in the dark for up to 40 min, where a series of vibrational bands can be identified: peak i (3555 cm<sup>-1</sup>) due to the N-H stretch, peak ii (3360 cm<sup>-1</sup>) due to adsorbed-OH, peak iii (2874 cm<sup>-1</sup>) due to the NH<sub>4</sub>+ stretching vibration, peak iv (2359 cm<sup>-1</sup>) due to adsorbed CO<sub>2</sub>, peak v (1624 cm<sup>-1</sup>) due to adsorbed N<sub>2</sub>, and peak vi (1557 cm<sup>-1</sup>) due to adsorbed NH<sub>3</sub>. The intensity of these vibrational bands grew with adsorption time. Upon visible light photoirradiation (Figure 5b), one can see a significant and fast change in the IR signals. Specifically, peaks i, iii, and iv were markedly weakened, while peaks ii, v, and vi were obviously enhanced, suggesting an enhanced adsorption of N2 and the conversion of N-H to NH<sub>3</sub>.50,51

Figure 5c shows the in situ IR spectra during photocatalytic nitrogen fixation for up to 35 min. It can be seen that with increasing photoirradiation time the IR signals became intensified accordingly. In comparison with data collected in the dark (Figure 5a), peaks i and iii were significantly strengthened, but peak v (adsorbed  $N_2$ ) was obviously weakened, suggesting the effective cleavage of the  $N \equiv N$  bond and the subsequent formation of  $NH_4^+$ . In fact, the N-H bending vibrations (peaks iv and vii) increased in intensity after prolonged photoirradiation. <sup>27,52–54</sup> Figure 5d compares

the IR spectra acquired after 35 min of visible light illumination before the light was turned off. In comparison with the results in Figure 5b, one can see that upon the switching off of the light source, peaks i and ii remained virtually unchanged, and peaks iii, iv, and vi increased significantly, indicating an increasing concentration of N–H bonds and a large number of N<sub>2</sub> molecules adsorbed on the catalyst surface. Taken together, these results suggest that the ready adsorption of nitrogen onto Bi<sub>5</sub>O<sub>7</sub>Br-40 was likely responsible for the excellent nitrogen fixation performance. This can be ascribed to the high concentration of OVs in the sample (Figure 3), as manifested below in DFT calculations.

In order to examine the influence of OVs on the nitrogen fixation performance, DFT calculations were performed with three structural models: pristine  $Bi_5O_7Br$ , anoxic  $Bi_5O_7Br-O$ , and oxygen-enriched  $Bi_5O_7Br+O$  (Figure 6a). From the reaction energy diagram of the nitrogen fixation pathway of  $*N_2 \rightarrow *NNH \rightarrow *NNH_2 \rightarrow *NNH_3 \rightarrow *N + NH_3 \rightarrow *NH \rightarrow *NH_2 \rightarrow *NH_3 \rightarrow NH_3$  (Figure 6b,c), one can see that  $N_2$  adsorption on  $Bi_5O_7Br-O$  was indeed favored by the most negative adsorption free energy (-0.017 eV) for the initial  $N_2$  activation  $(*N_2)$ , in comparison to -0.008 eV for pristine  $Bi_5O_7Br$  and -0.001 eV for pristine  $Bi_5O_7Br+O$  (Figure 6d).

Furthermore, on the three catalysts, one can see that the  $*N-NH_2 \rightarrow *N-NH_3$  step exhibits the greatest energy barrier (Figure 6b), suggesting that this is the rate-determining step in the reaction pathway (Figure 6c),<sup>54</sup> and this energy barrier varies among the samples, decreasing from 3.213 eV for Bi<sub>5</sub>O<sub>7</sub>Br+O to 3.019 eV for Bi<sub>5</sub>O<sub>7</sub>Br and to 2.963 eV for Bi<sub>5</sub>O<sub>7</sub>Br-O. In addition, the adsorption free energy of the \*NH<sub>2</sub> product increases from -1.698 eV for Bi<sub>5</sub>O<sub>7</sub>Br+O to −1.717 eV for Bi<sub>5</sub>O<sub>7</sub>Br and −1.969 eV for Bi<sub>5</sub>O<sub>7</sub>Br−O. Taken together, these results suggest that the oxygen-deficient Bi<sub>5</sub>O<sub>7</sub>Br-O represents the optimal catalyst for nitrogen adsorption and activation and hence ammonia synthesis. Note that whereas hydrazine (H2NNH2) is a common intermediate in the electrochemical reduction of nitrogen for ammonia synthesis, no such species was detected experimentally in the present study.

In summary, these results show that photocatalytic  $N_2$  fixation by  $Bi_5O_7Br$ ,  $N_2+6H^++6e^- \rightarrow 2NH_3$ , most likely involves four major steps (Figure 7): (i) under visible light irradiation, part of the O atoms escape in the form of  $O_2$  from the  $Bi_5O_7Br$  surface, creating sufficient surface OVs; (ii)  $N_2$  is chemisorbed and activated on the OVs; (iii) the photoexcited

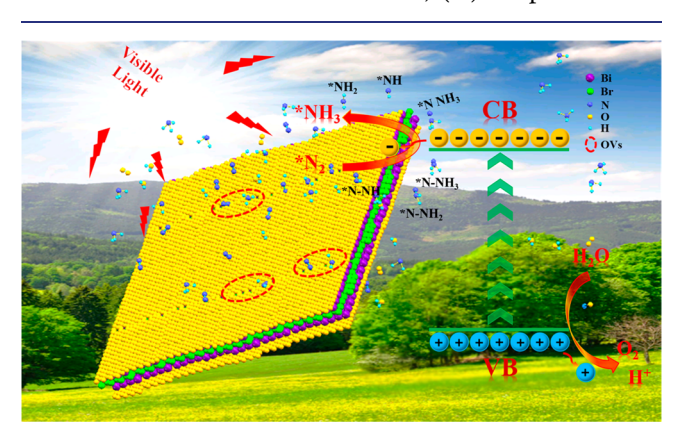


**Figure 7.** Schematic diagram of photocatalytic nitrogen fixation catalyzed by  ${\rm Bi}_5{\rm O}_7{\rm Br}$ .

electrons are injected into the activated  $N_2$  and reduce it to  $NH_3$ , which is dissolved in water in the form of  $NH_4^+$ ; and (iv) after reaction, the photoinduced OVs are refilled by capturing O from water, leading to a good recovery to the original stable OV-free composition.  $^{27,57,58}$ 

## CONCLUSIONS

In this study, a series of Bi<sub>5</sub>O<sub>7</sub>Br catalysts were prepared by a facile thermal precipitation process at different temperatures and exhibited excellent photocatalytic activity toward nitrogen fixation to ammonia. Among these, the sample prepared at 40 °C showed the best performance, which exhibited nanotubular morphology, a large specific surface area (>100 m<sup>2</sup>g<sup>-1</sup>), a suitable absorption edge, maximum photocurrent, a high concentration of O2-, and abundant OVs under photoirradiation. In situ infrared spectroscopic measurements showed that the unique Bi<sub>5</sub>O<sub>7</sub>Br-40 morphological and electronic characteristics facilitated the adsorption and activation of N<sub>2</sub> and the subsequent formation of NH<sub>3</sub>, consistent with results from DFT calculations. Results from this study indicate that Bi<sub>5</sub>O<sub>7</sub>Br nanostructures may be exploited as effective photocatalysts toward the fixation of nitrogen to ammonia under visible light irradiation, a unique technology toward a sustainable future. 59-62

## ASSOCIATED CONTENT

## **Supporting Information**

The Supporting Information is available free of charge at https://pubs.acs.org/doi/10.1021/jacs.0c05097.

Additional experimental data (PDF)

#### AUTHOR INFORMATION

#### **Corresponding Authors**

Qiang Wang — Laboratory for Micro-sized Functional Materials & College of Elementary Education and Department of Chemistry, Capital Normal University, Beijing 100048, P. R. China; orcid.org/0000-0002-9118-5615; Email: qwchem@gmail.com

Shaowei Chen — Department of Chemistry and Biochemistry, University of California, Santa Cruz, California 95064, United States; orcid.org/0000-0002-3668-8551; Email: shaowei@ucsc.edu

Wen Liu — Beijing Innovation Center for Engineering Science and Advanced Technology (BIC-ESAT) and Key Laboratory of Water and Sediment Sciences, Ministry of Education, College of Environmental Sciences and Engineering, Peking University, Beijing 100871, P. R. China; ⊙ orcid.org/0000-0002-6787-2431; Email: wen.liu@pku.edu.cn

Yujie Xiong — Hefei National Laboratory for Physical Sciences at the Microscale, Collaborative Innovation Center of Chemistry for Energy Materials (iChEM), School of Chemistry and Materials Science, University of Science and Technology of China, Hefei, Anhui 230026, P. R. China; ⊙ orcid.org/0000-0002-1995-8257; Email: yjxiong@ustc.edu.cn

#### Authors

Peishen Li – Laboratory for Micro-sized Functional Materials & College of Elementary Education and Department of Chemistry, Capital Normal University, Beijing 100048, P. R. China

Ziang Zhou – Laboratory for Micro-sized Functional Materials & College of Elementary Education and Department of

- Chemistry, Capital Normal University, Beijing 100048, P. R. China
- Ming Guo Laboratory for Micro-sized Functional Materials & College of Elementary Education and Department of Chemistry, Capital Normal University, Beijing 100048, P. R. China
- Jingxiang Low Hefei National Laboratory for Physical Sciences at the Microscale, Collaborative Innovation Center of Chemistry for Energy Materials (iChEM), School of Chemistry and Materials Science, University of Science and Technology of China, Hefei, Anhui 230026, P. R. China
- Ran Long Hefei National Laboratory for Physical Sciences at the Microscale, Collaborative Innovation Center of Chemistry for Energy Materials (iChEM), School of Chemistry and Materials Science, University of Science and Technology of China, Hefei, Anhui 230026, P. R. China
- Peiren Ding Laboratory for Micro-sized Functional Materials & College of Elementary Education and Department of Chemistry, Capital Normal University, Beijing 100048, P. R. China
- Yunyun Wu Laboratory for Micro-sized Functional Materials & College of Elementary Education and Department of Chemistry, Capital Normal University, Beijing 100048, P. R. China

Complete contact information is available at: https://pubs.acs.org/10.1021/jacs.0c05097

#### **Notes**

The authors declare no competing financial interest.

## ACKNOWLEDGMENTS

This work was supported by the National Natural Science Foundation of China (NSFC; 21471103, 51631001, 21725102, and 21906001), the Scientific Research Base Development Program, and the Science and the Technology Innovation Service Ability Construction Project of Beijing Municipal Commission of Education. S.C. acknowledges support by the U.S. National Science Foundation (CBET-1848841, CHE-1900235). DRIFTS measurements were performed at the Infra-red Spectroscopy and Microspectroscopy Endstation (BL01B) in the National Synchrotron Radiation Laboratory (NSRL) in Hefei, China.

## **■** REFERENCES

- (1) Yasin, A. S.; Liu, B.; Wu, N.; Musho, T. Density Functional Theory Evaluation of Cation-Doped Bismuth Molybdenum Oxide Photocatalysts for Nitrogen Fixation. *Comput. Mater. Sci.* **2019**, *158*, 65–75.
- (2) Jia, H. P.; Quadrelli, E. A. Mechanistic Aspects of Dinitrogen Cleavage and Hydrogenation to Produce Ammonia in Catalysis and Organometallic Chemistry: Relevance of Metal Hydride Bonds and Dihydrogen. *Chem. Soc. Rev.* **2014**, *43*, 547–64.
- (3) MacKay, B. A.; Fryzuk, M. D. Dinitrogen Coordination Chemistry: on the Biomimetic Borderlands. *Chem. Rev.* **2004**, *104*, 385–402.
- (4) Gao, X.; Shang, Y.; Liu, L.; Fu, F. Chemisorption-enhanced Photocatalytic Nitrogen Fixation Via 2D Ultrathin p-n Heterojunction  $AgCl/\delta$ -Bi<sub>2</sub>O<sub>3</sub> Nanosheets. *J. Catal.* **2019**, *371*, 71–80.
- (5) Li, J.; Niu, A.; Lu, C. J.; Zhang, J. H.; Junaid, M.; Strauss, P. R.; Xiao, P.; Wang, X.; Ren, Y. W.; Pei, D. S. A Novel Forward Osmosis System in Landfill Leachate Treatment for Removing Polycyclic Aromatic Hydrocarbons and for Direct Fertigation. *Chemosphere* 2017, 168, 112–121.
- (6) Hirakawa, H.; Hashimoto, M.; Shiraishi, Y.; Hirai, T. Photocatalytic Conversion of Nitrogen to Ammonia with Water on

- Surface Oxygen Vacancies of Titanium Dioxide. J. Am. Chem. Soc. 2017. 139, 10929–10936.
- (7) Wang, S.; Ichihara, F.; Pang, H.; Chen, H.; Ye, J. Nitrogen Fixation Reaction Derived from Nanostructured Catalytic Materials. *Adv. Funct. Mater.* **2018**, 28, 1803309.
- (8) Ababou-Girard, S.; Sabbah, H.; Fabre, B.; Zellama, K.; Solal, F.; Godet, C. Covalent Grafting of Organic Layers on Sputtered Amorphous Carbon: Surface Preparation and Coverage Density. *J. Phys. Chem. C* **2007**, *111*, 3099–3108.
- (9) Zhang, K.; Liu, C.; Huang, F.; Zheng, C.; Wang, W. Study of the Electronic Structure and Photocatalytic Activity of the BiOCl Photocatalyst. *Appl. Catal., B* **2006**, *68*, 125–129.
- (10) Lei, F.; Sun, Y.; Liu, K.; Gao, S.; Liang, L.; Pan, B.; Xie, Y. Oxygen Vacancies Confined in Ultrathin Indium Oxide Porous Sheets for Promoted Visible-light Water Splitting. *J. Am. Chem. Soc.* **2014**, 136, 6826–6829.
- (11) Zhao, K.; Zhang, L.; Wang, J.; Li, Q.; He, W.; Yin, J. J. Surface Structure-dependent Molecular Oxygen Activation of BiOCl Single-crystalline Nanosheets. *J. Am. Chem. Soc.* **2013**, *135*, 15750–15753.
- (12) Guan, M.; Xiao, C.; Zhang, J.; Fan, S.; An, R.; Cheng, Q.; Xie, J.; Zhou, M.; Ye, B.; Xie, Y. Vacancy Associates Promoting Solar-driven Photocatalytic Activity of Ultrathin Bismuth Oxychloride Nanosheets. J. Am. Chem. Soc. 2013, 135, 10411–10417.
- (13) Ye, L.; Zan, L.; Tian, L.; Peng, T.; Zhang, J. The {001} Facets-dependent High Photoactivity of BiOCl Nanosheets. *Chem. Commun.* (*Cambridge, U. K.*) **2011**, 47, 6951–6953.
- (14) Sun, Y.; Sun, Z.; Gao, S.; Cheng, H.; Liu, Q.; Piao, J.; Yao, T.; Wu, C.; Hu, S.; Wei, S.; Xie, Y. Fabrication of Flexible and Freestanding Zinc Chalcogenide Single Layers. *Nat. Commun.* **2012**, 3, 1057.
- (15) Jiang, J.; Zhao, K.; Xiao, X.; Zhang, L. Synthesis and Facet-dependent Photoreactivity of BiOCl Single-crystalline Nanosheets. *J. Am. Chem. Soc.* **2012**, *134*, 4473–4476.
- (16) Abbott, N. L.; Rolison, D. R.; Whitesides, G. M. Combining Micromachining and Molecular Self-Assembly to Fabricate Microelectrodes. *Langmuir* 1994, 10, 2672–2682.
- (17) Rinaldi, A.; Araneo, R.; Celozzi, S.; Pea, M.; Notargiacomo, A. The Clash of Mechanical and Electrical Size-effects in ZnO Nanowires and a Double Power Law Approach to Elastic Strain Engineering of Piezoelectric and Piezotronic Devices. *Adv. Mater.* **2014**, *26*, 5976–5985.
- (18) Zhou, P.; Yu, J.; Jaroniec, M. All-Solid-State Z-Scheme Photocatalytic Systems. *Adv. Mater.* **2014**, *26*, 4920–4935.
- (19) Xia, J.; Yin, S.; Li, H.; Xu, H.; Xu, L.; Xu, Y. Improved Visible Light Photocatalytic Activity of Sphere-like BiOBr Hollow and Porous Structures Synthesized Via a Reactable Ionic Liquid. *Dalton Trans* **2011**, *40*, 5249–5258.
- (20) Huo, Y.; Zhang, J.; Miao, M.; Jin, Y. Solvothermal Synthesis of Flower-like BiOBr Microspheres with Highly Visible-light Photocatalytic Performances. *Appl. Catal., B* **2012**, *111–112*, 334–341.
- (21) Fan, Z.; Zhao, Y.; Zhai, W.; Qiu, L.; Li, H.; Hoffmann, M. R. Facet-dependent Performance of BiOBr for Photocatalytic Reduction of Cr(vi). RSC Adv. 2016, 6, 2028–2031.
- (22) Yang, C. T.; Lee, W. W.; Lin, H. P.; Dai, Y. M.; Chi, H. T.; Chen, C. C. A Novel Heterojunction Photocatalyst,  $Bi_2SiO_5/g-C_3N_4$ : Synthesis, Characterization, Photocatalytic Activity, and Mechanism. *RSC Adv.* **2016**, *6*, 40664–40675.
- (23) Di, J.; Xia, J.; Yin, S.; Xu, H.; He, M.; Li, H.; Xu, L.; Jiang, Y. A g- $C_3N_4/BiOBr$  Visible-light-driven Composite: Synthesis Via a Reactable Ionic Liquid and Improved Photocatalytic Activity. *RSC Adv.* **2013**, *3*, 19624–19631.
- (24) Cheng, H.; Huang, B.; Wang, P.; Wang, Z.; Lou, Z.; Wang, J.; Qin, X.; Zhang, X.; Dai, Y. In Situ Ion Exchange Synthesis of the Novel Ag/AgBr/BiOBr Hybrid with Highly Efficient Decontamination of Pollutants. *Chem. Commun.* (Cambridge, U. K.) 2011, 47, 7054–7056.
- (25) Di, J.; Xia, J.; Ge, Y.; Xu, L.; Xu, H.; Chen, J.; He, M.; Li, H. Facile Fabrication and Enhanced Visible Light Photocatalytic Activity

- of Few-layer MoS<sub>2</sub> Coupled BiOBr Microspheres. *Dalton Trans* **2014**, 43, 15429–38.
- (26) Lin, L.; Wang, Y.; Huang, M.; Chen, D. Immobilization of BiOBr/BiOI Hierarchical Microspheres on Fly Ash Cenospheres as Visible Light Photocatalysts. *Aust. J. Chem.* **2016**, *69*, 119–125.
- (27) Wang, S.; Hai, X.; Ding, X.; Chang, K.; Xiang, Y.; Meng, X.; Yang, Z.; Chen, H.; Ye, J. Light-Switchable Oxygen Vacancies in Ultrafine Bi<sub>5</sub>O<sub>7</sub>Br Nanotubes for Boosting Solar-Driven Nitrogen Fixation in Pure Water. *Adv. Mater.* **2017**, *29*, 1701774.
- (28) Segall, M. D.; Lindan, P. J. D.; Probert, M. J.; Pickard, C. J.; Hasnip, P. J.; Clark, S. J.; Payne, M. C. First-principles Simulation: Ideas, Illustrations and the CASTEP Code. *J. Phys.: Condens. Matter* **2002**, *14*, 2717–2744.
- (29) Perdew, J. P.; Ruzsinszky, A.; Csonka, G. I.; Vydrov, O. A.; Scuseria, G. E.; Constantin, L. A.; Zhou, X.; Burke, K. Restoring the Density-gradient Expansion for Exchange in Solids and Surfaces. *Phys. Rev. Lett.* **2008**, *100*, 136406.
- (30) Dias, J. R.; Milne, G. W. A. Chemical Applications of Graph Theory. *J. Chem. Inf. Model.* **1992**, 32, 1.
- (31) Kresse, G.; Hafner, J. Norm-conserving and Ultrasoft Pseudopotentials for First-row and Transition Elements. *J. Phys.: Condens. Matter* **1994**, *6*, 8245.
- (32) Wu, D.; Yue, S.; Wang, W.; An, T.; Li, G.; Yip, H. Y.; Zhao, H.; Wong, P. K. Boron Doped BiOBr Nanosheets with Enhanced Photocatalytic Inactivation of Escherichia Coli. *Appl. Catal., B* **2016**, 192, 35–45.
- (33) Di, J.; Xia, J.; Ji, M.; Yin, S.; Li, H.; Xu, H.; Zhang, Q.; Li, H. Controllable Synthesis of Bi<sub>4</sub>O<sub>5</sub>Br<sub>2</sub> Ultrathin Nanosheets for Photocatalytic Removal of Ciprofloxacin and Mechanism Insight. *J. Mater. Chem. A* **2015**, 3, 15108–15118.
- (34) Su, Y.; Ding, C.; Dang, Y.; Wang, H.; Ye, L.; Jin, X.; Xie, H.; Liu, C. First Hydrothermal Synthesis of Bi<sub>5</sub>O<sub>7</sub>Br and Its Photocatalytic Properties for Molecular Oxygen Activation and RhB Degradation. *Appl. Surf. Sci.* **2015**, 346, 311–316.
- (35) Keller, E.; Kramer, V. Bi<sub>5</sub>O<sub>7</sub>Br and Its Structural Relation to Alpha-Bi<sub>5</sub>O<sub>7</sub>I. *Acta Crystallogr.* C **2007**, *63*, 109–111.
- (36) Zhang, X.; Pei, C.; Chang, X.; Chen, S.; Liu, R.; Zhao, Z.; Mu, R.; Gong, J., FeO<sub>6</sub> Octahedral Distortion Activates Lattice Oxygen in Perovskite Ferrite for Methane Partial Oxidation Coupled with CO<sub>2</sub>-Splitting. *J. Am. Chem. Soc.* **2020**, DOI: 10.1021/jacs.0c04643.
- (37) Liu, G.; Niu, P.; Sun, C. H.; Smith, S. C.; Chen, Z. G.; Lu, G. Q.; Cheng, H. M. Unique Electronic Structure Induced High Photoreactivity of Sulfur-Doped Graphitic C<sub>3</sub>N<sub>4</sub>. *J. Am. Chem. Soc.* **2010**, *132*, 11642–11648.
- (38) Pan, J.; Liu, G.; Lu, G. Q.; Cheng, H. M. On the True Photoreactivity Order of {001}, {010}, and {101} Facets of Anatase TiO<sub>2</sub> Crystals. *Angew. Chem., Int. Ed.* **2011**, *50*, 2133–2137.
- (39) Chang, K.; Hai, X.; Pang, H.; Zhang, H.; Shi, L.; Liu, G.; Liu, H.; Zhao, G.; Li, M.; Ye, J. Targeted Synthesis of 2H- and 1T-Phase MoS<sub>2</sub> Monolayers for Catalytic Hydrogen Evolution. *Adv. Mater.* **2016**, 28, 10033–10041.
- (40) Di, J.; Xia, J.; Ji, M.; Li, H.; Xu, H.; Li, H.; Chen, R. The Synergistic Role of Carbon Quantum Dots for the Improved Photocatalytic Performance of Bi<sub>2</sub>MoO<sub>6</sub>. *Nanoscale* **2015**, 7, 11433–11443.
- (41) Abgrall, P.; Nguyen, N. T. Nanofluidic Devices and Their Applications. *Anal. Chem.* **2008**, *80*, 2326–2341.
- (42) Ma, J.; Wang, K.; Wang, C.; Chen, X.; Zhu, W.; Zhu, G.; Yao, W.; Zhu, Y. Photocatalysis-self-Fenton System with High-fluent Degradation and High Mineralization Ability. *Appl. Catal., B* **2020**, 276, 119150.
- (43) Abid, J. P.; Nappa, J.; Girault, H. H.; Brevet, P. F. Pure Surface Plasmon Resonance Enhancement of the First Hyperpolarizability of Gold Core-silver Shell Nanoparticles. *J. Chem. Phys.* **2004**, *121*, 12577–12582.
- (44) Hai, X.; Chang, K.; Pang, H.; Li, M.; Li, P.; Liu, H.; Shi, L.; Ye, J. Engineering the Edges of MoS<sub>2</sub> (WS<sub>2</sub>) Crystals for Direct Exfoliation into Monolayers in Polar Micromolecular Solvents. *J. Am. Chem. Soc.* **2016**, *138*, 14962–14969.

- (45) Li, P.; Guo, M.; Wang, Q.; Li, Z.; Wang, C.; Chen, N.; Wang, C. C.; Wan, C.; Chen, S. Controllable Synthesis of Cerium Zirconium Oxide Nanocomposites and their Application for Photocatalytic Degradation of Sulfonamides. *Appl. Catal., B* **2019**, 259, 118107.
- (46) Zhu, W.; Sun, F.; Goei, R.; Zhou, Y. Facile Fabrication of RGO-WO<sub>3</sub> Composites for Effective Visible Light Photocatalytic Degradation of Sulfamethoxazole. *Appl. Catal., B* **2017**, *207*, 93–102.
- (47) Feng, X.; Chen, Y.; Qin, Z.; Wang, M.; Guo, L. Facile Fabrication of Sandwich Structured WO<sub>3</sub> Nanoplate Arrays for Efficient Photoelectrochemical Water Splitting. *ACS Appl. Mater. Interfaces* **2016**, *8*, 18089–96.
- (48) McCrory, C. C.; Jung, S.; Ferrer, I. M.; Chatman, S. M.; Peters, J. C.; Jaramillo, T. F. Benchmarking Hydrogen Evolving Reaction and Oxygen Evolving Reaction Electrocatalysts for Solar Water Splitting Devices. J. Am. Chem. Soc. 2015, 137, 4347–4357.
- (49) Bu, X.; Gao, Y.; Zhang, S.; Tian, Y. Amorphous Cerium Phosphate on P-doped  $Fe_2O_3$  Nanosheets for Efficient Photoelectrochemical Water Oxidation. *Chem. Eng. J.* **2019**, 355, 910–919.
- (50) Shi, L.; Li, Z.; Ju, L.; Carrasco-Pena, A.; Orlovskaya, N.; Zhou, H.; Yang, Y. Promoted Nitrogen Photofixation over Periodic WS<sub>2</sub>@ TiO<sub>2</sub> Nanoporous Film. *J. Mater. Chem. A* **2020**, *8*, 1059–1065.
- (51) Kong, Y.; Lv, C.; Zhang, C.; Chen, G. Cyano Group Modified g-C3N4: Molten Salt Method Achievement and Promoted Photocatalytic Nitrogen Fixation Activity. *Appl. Surf. Sci.* **2020**, *515*, 146009.
- (52) Abramson, S.; Srithammavanh, L.; Siaugue, J. M.; Horner, O.; Xu, X. Z.; Cabuil, V. Nanometric Core-shell-shell Gamma-Fe<sub>2</sub>O<sub>3</sub>/SiO<sub>2</sub>/TiO<sub>2</sub> Particles. *J. Nanopart. Res.* **2009**, *11*, 459–465.
- (53) Abril, O.; Crans, D. C.; Whitesides, G. M. Practical Enzymatic-Synthesis of Adenosine 5'-O-(3-Thiotriphosphate) (Atp-Gamma-S). *J. Org. Chem.* **1984**, 49, 1360–1364.
- (54) Zhang, N.; Jalil, A.; Wu, D.; Chen, S.; Liu, Y.; Gao, C.; Ye, W.; Qi, Z.; Ju, H.; Wang, C.; Wu, X.; Song, L.; Zhu, J.; Xiong, Y. Refining Defect States in W<sub>18</sub>O<sub>49</sub> by Mo Doping: A Strategy for Tuning N<sub>2</sub> Activation towards Solar-Driven Nitrogen Fixation. *J. Am. Chem. Soc.* **2018**, *140*, 9434–9443.
- (55) Yuzawa, H.; Mori, T.; Itoh, H.; Yoshida, H. Reaction Mechanism of Ammonia Decomposition to Nitrogen and Hydrogen over Metal Loaded Titanium Oxide Photocatalyst. *J. Phys. Chem. C* **2012**, *116*, 4126–4136.
- (56) Shipman, M. A.; Symes, M. D. Recent Progress Towards the Electrosynthesis of Ammonia from Sustainable Resources. *Catal. Today* **2017**, *286*, 57–68.
- (57) Tan, H.; Zhao, Z.; Zhu, W.; Coker, E. N.; Li, B.; Zheng, M.; Yu, W.; Fan, H.; Sun, Z. Oxygen Vacancy Enhanced Photocatalytic Activity of Pervoskite SrTiO<sub>3.</sub> ACS Appl. Mater. Interfaces **2014**, 6, 19184–19190.
- (58) Zhang, L.; Wang, W.; Jiang, D.; Gao, E.; Sun, S. Photoreduction of  $\rm CO_2$  on BiOCl Nanoplates with the Assistance of Photoinduced Oxygen Vacancies. *Nano Res.* **2015**, *8*, 821–831.
- (59) Cheng, H.; Ding, L. X.; Chen, G. F.; Zhang, L.; Xue, J.; Wang, H. Molybdenum Carbide Nanodots Enable Efficient Electrocatalytic Nitrogen Fixation under Ambient Conditions. *Adv. Mater.* **2018**, *30*, No. 1870350.
- (60) Wu, S.; Tan, X.; Liu, K.; Lei, J.; Wang, L.; Zhang, J.  $TiO_2(B)$  Nanotubes with Ultrathin Shell for Highly Efficient Photocatalytic Fixation of Nitrogen. *Catal. Today* **2019**, 335, 214–220.
- (61) Xiao, C.; Zhang, L.; Wang, K.; Wang, H.; Zhou, Y.; Wang, W. A New Approach to Enhance Photocatalytic Nitrogen Fixation Performance Via Phosphate-bridge: A Case Study of SiW<sub>12</sub>/K-C<sub>3</sub>N<sub>4</sub>. Appl. Catal., B **2018**, 239, 260–267.
- (62) Lv, C.; Yan, C.; Chen, G.; Ding, Y.; Sun, J.; Zhou, Y.; Yu, G. An Amorphous Noble-Metal-Free Electrocatalyst that Enables Nitrogen Fixation under Ambient Conditions. *Angew. Chem., Int. Ed.* **2018**, *57*, 6073–6076.